# Experimental Investigation of Smoothing by Spectral Dispersion

In the direct-drive approach to inertial confinement fusion (ICF), capsules are irradiated directly by a large number of symmetrically arranged laser beams.[1,2] Nonuniformities in the laser irradiation may seed the Rayleigh–Taylor hydrodynamic instability, which degrades target performance;[3] therefore, a combination of beam-smoothing techniques is employed to achieve the high irradiation uniformity required for direct-drive laser-fusion experiments. These techniques, which include two-dimensional smoothing by spectral dispersion (2-D SSD),[4–6] distributed phase plates (DPP's),[7,8] polarization smoothing (DPR's),[9–11] and multiple-beam overlap, will also be implemented on the 1.8-MJ, 351-nm, 192-beam National Ignition Facility (NIF),[12] which is currently under construction at the Lawrence Livermore National Laboratory. Direct-drive laser fusion requires a high degree of laser-irradiation uniformity on target: the rms irradiation nonuniformity must be below 1% when the laser intensity has been averaged over a few hundred picoseconds.[2,5]

Characterization of the laser-irradiation nonuniformity is essential for ICF research since the efficiency with which the nonuniformities in the laser-irradiation imprint target mass perturbations (i.e., laser imprint) depends on the early-time intensity history and the spatial wavelength of the nonuniformity.[13] The strategy of 2-D SSD with phase plates, which is the preferred mechanism for reducing laser-beam irradiation nonuniformity in glass lasers, is to vary the interference (speckle) pattern of the phase plate on a time scale that is short compared to the characteristic hydrodynamic response time of the target (i.e., imprinting time). (An alternate technique, ISI, has been developed for KrF lasers.[14]) Predictions show that 2-D SSD smoothing with $\Delta\nu_{UV} \approx 1$ THz will smooth the spherical-harmonic modes of $\ell = 20$ through 150 to acceptable levels for ICF.[5] The bandwidth on OMEGA[15] will be increased from 0.2 to 1 THz during this year, which will decrease the smoothing time by a factor of 5.

In this research the temporal rate of beam smoothing produced by 2-D SSD with the current bandwidth of $\Delta\nu_{UV} \approx 0.2$ THz is quantified by analyzing measured ultraviolet equivalent-target-plane (UVETP) images of a single OMEGA laser beam. The next three sections describe (1) laser-beam smoothing with 2-D SSD and phase plates, (2) 2-D SSD model calculations, and (3) the diagnostic used to record UVETP images of laser pulses having constant peak power and varying duration (100 ps to 3.5 ns). Power spectra calculated from the measured UVETP images along with the measured smoothing rate of 2-D SSD are presented and compared with theoretical predictions in the **Experimental Results and Analysis** section. This work shows that the theoretical predictions of 2-D SSD laser-beam smoothing are in excellent agreement with the measured temporal smoothing rates.

## Background

Smoothing of laser beams using SSD has been described in Ref. 4. On OMEGA the phase plates are placed before the focusing lens and produce far-field spots with highly reproducible spatial intensity envelopes and speckle distributions. Smoothing by spectral dispersion is achieved by frequency modulating the phase of a laser beam, wavelength dispersing the beam, and passing it through a phase plate so that the spectral components are separated in the target plane by at least one-half the beam's diffraction-limited width. The reduction in laser-irradiation nonuniformity is wavelength dependent. The longest wavelength of nonuniformity that can be smoothed by SSD is twice the maximum spatial shift $S_{max} = F\Delta\theta$ of the speckle pattern that can be produced by the laser, where $\Delta\theta$ is the angular spread of the wavelength-dispersed light propagating through the laser and $F$ is the focal length of the OMEGA lens. (The ultimate limit of $S$ is given by the maximum allowable angular spread in the spatial filter in the laser system.) Thus, spherical-harmonic modes of nonuniformity down to $l_{cut} = 2\pi R/(2S_{max})$, where $R$ is the target radius, can be smoothed with 2-D SSD.[5] Spherical targets on OMEGA have $R \simeq 500$ $\mu$m, and the present 2-D SSD system has $S_{max} = 100$ $\mu$m; hence $l_{cut} = 16$.

## Model Calculations

The time-integrated far field is calculated by temporal integration of the modulus squared of a two-dimensional

spatial Fourier transform of the UV near field. The complex-valued electric field that describes the UV near field can be written as

$$E(x,y,t) \equiv E_0(x,y,t)e^{i\phi_{2\text{-D SSD}}(x,y,t)}e^{i\phi_B(x,y,t)}e^{i\phi_{\text{DPP}}(x,y)}, \quad (1)$$

where $E_0(x,y,t)$ defines the temporal and spatial beam shapes, $\phi_{2\text{-D SSD}}(x,y,t)$ is the 2-D SSD phase contribution, $\phi_B(x,y,t)$ is the intensity-dependent phase contribution of the *B*-integral,[16] and $\phi_{\text{DPP}}(x,y)$ is the static phase-plate contribution, which depends on the particular phase-plate design.

The spatially and temporally varying phase due to 2-D SSD is[17]

$$\phi_{2\text{-D SSD}}(x,y,t) \equiv 3\delta_{Mx}\sin\left[\omega_{Mx}\left(t+\xi_x x\right)\right] + 3\delta_{My}\sin\left[\omega_{My}\left(t+\xi_y y\right)\right], \quad (2)$$

where the *x* and *y* subscripts denote the two smoothing dimensions, $\delta_{Mx,y}$ is the modulation depth, $\nu_{Mx,y} = \omega_{Mx,y}/2\pi$ is the RF modulation frequency, and $\xi_{x,y}$ is the angular grating dispersion. The factor of 3 in Eq. (2) indicates that the electric field has undergone frequency tripling from the IR to UV. The 2-D SSD system parameters on OMEGA for the UVETP measurements are $\delta_{Mx} = 5.12$, $\nu_{Mx} \equiv 3.3$ GHz, $\xi_x = 1.11$ ns/m, $\Delta\lambda_{Mx} = 1.25$ Å, $\delta_{My} = 7.89$, $\nu_{My} \equiv 3.0$ GHz, $\xi_y = 1.11$ ns/m, and $\Delta\lambda_{My} = 1.75$ Å, assuming a nominal beam diameter of 27.5 cm. The modulation depths and the bandwidths are given for the IR. The maximum angular spread $\Delta\theta$ is given by $\Delta\theta = \xi(c/\lambda)\Delta\lambda$, where *c* is the speed of light and $\lambda = 1053$ nm. Cases without frequency modulation are modeled by setting modulation depths equal to zero, i.e., $\delta_{Mx} = 0$ and $\delta_{My} = 0$.

Our simulations indicate that *B*-integral effects are negligible for all cases except when the frequency modulation is turned off.

**UVETP Diagnostic**

The layout of the diagnostic used to acquire the UVETP images of a single OMEGA beam is shown in Fig. 79.34. Time-integrated UVETP images were recorded with a CCD camera. All of the measurements presented in this article exploit the low noise level and the large dynamic range of the CCD to extract power spectra from the UVETP images with negligible noise levels. The UV-sensitive CCD camera is a back-thinned SITe 003B chip in a Photometrics Series 300 camera.[18] The sensor has an array of 1024 × 1024 photosensitive elements with a pixel size of 24 $\mu$m × 24 $\mu$m. The spatial sampling rate is ~2 pixels/$\mu$m, which is approximately five times the *f*-number-limited spatial frequency $f_0 \equiv \Delta/\lambda F$, where *D* is the beam diameter of the OMEGA lens and $\lambda = 351$ nm.

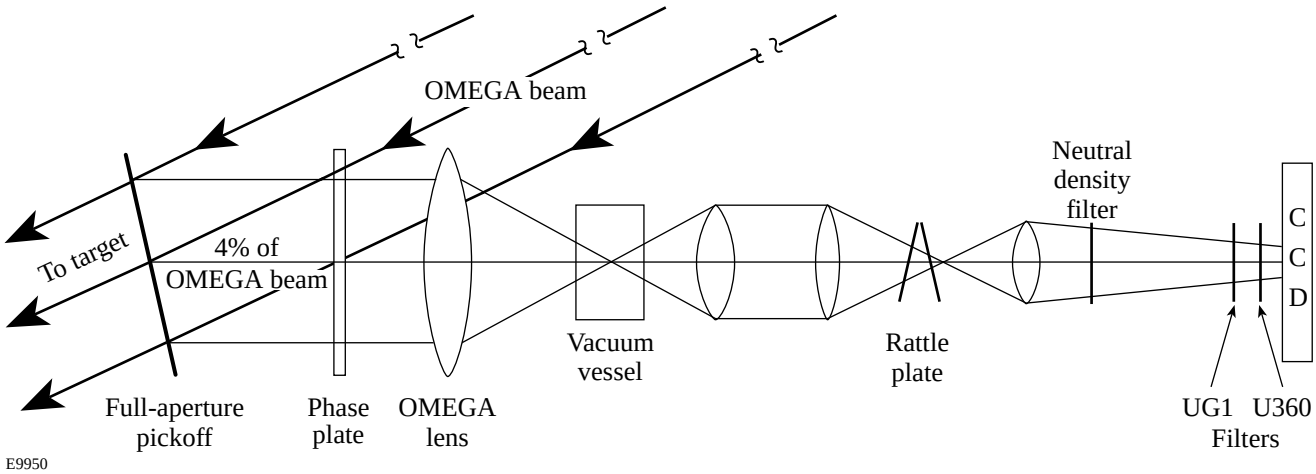


Figure 79.34
Schematic of the UVETP diagnostic. The on-target spot size is magnified by $M = 46$ on the CCD camera.

A full-aperture optical wedge in one of the 60 laser beams (BL-19) directs 4% of the laser light to an OMEGA focusing lens (see Fig. 79.34). The phase plate is placed directly in front of the lens, mimicking the target/beam configuration. The beam is brought through focus in a vacuum tube, down collimated with a doublet lens, brought to focus with a 2-m lens, and relayed to the CCD camera with the final lens. The beam intensity is reduced with three 4% reflections (not shown in Fig. 79.34) and the fifth-order reflection of a rattle plate (consisting of two surfaces with $R$ = 70% per surface). The optical background is reduced to negligible levels with a light shield surrounding the CCD optics and the CCD camera. The light levels incident on the CCD are optimized by attenuating the beam with a neutral density filter that is placed after the final lens. Background-visible and IR signals are blocked with broadband UG1[19] and U360[20] UV bandpass filters mounted in front of the CCD camera. Compared with the laser spot size on target the UVETP image on the CCD camera is magnified by a factor of ~46.

Small-scale and whole-beam *B*-integral effects were found to provide smoothing of beams without frequency modulation. (The detailed analysis of beams without frequency modulation will be presented in a later publication.) A UVETP image of a laser pulse with zero accumulated *B*-integral (*B*-integral <1.0 rad in the UV) and no frequency modulation was measured to quantify the amount of beam smoothing due to the *B*-integral at higher laser powers. The power spectrum is the azimuthal sum at each spatial frequency of the square of the Fourier amplitudes. The power spectrum is normalized to the dc component, and the single-beam irradiation nonuniformity $\sigma_{rms}$ is defined as the square root of the ratio of the power in the high frequencies (i.e., $k \geq 0.04\ \mu m^{-1}$ in the OMEGA target plane) to the power in the low frequencies (i.e., $k < 0.04\ \mu m^{-1}$). The highest (cutoff) wave number $k = 2.68\ \mu m^{-1}$ corresponds to the *f*-number-limited spatial frequency. A spectrum for a zero-*B*-integral laser pulse without frequency modulation is presented in Fig. 79.35 and its irradiation nonuniformity, $\sigma_{rms}$ = 93.4%, is the highest measured under any condition and is near the 100% value expected from theory. The theoretical power spectrum simulated with the time-dependent code (described in the previous section) is also shown in Fig. 79.35 and includes the spatiotemporal near-field irradiance and small-scale and whole-beam *B*-integral effects. The higher value of $\sigma_{rms}$ predicted by the model is caused by the discrepancy between the model and the measurement in the low wave numbers (see Fig. 79.35). Nevertheless, the predicted speckle structure shows excellent agreement with the measurement; hence, the zero accumulated *B*-integral shot serves as a calibration that demonstrates the capability of the UVETP diagnostic to measure highly modulated spatial intensity profiles of pulses with no frequency modulation.

**Experimental Results and Analysis**

Measured UVETP images of 3.5-ns square laser pulses without frequency modulation and with 2-D SSD are presented in Figs. 79.36(a) and Fig 79.36(b), respectively. These images qualitatively illustrate the effect of laser-beam smoothing with 2-D SSD. The images with 2-D SSD show a smooth spatial intensity envelope [see single pixel lineout overplotted on

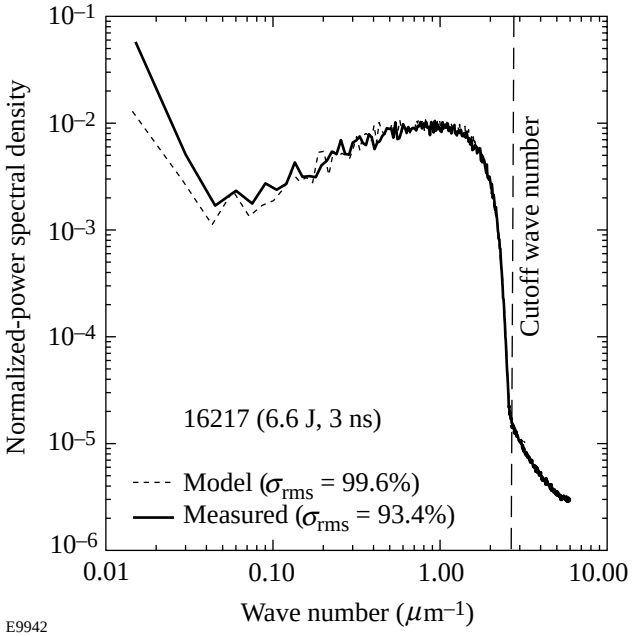


Figure 79.35
Power spectra obtained from a UVETP image of a laser pulse with zero accumulated *B*-integral (*B*-integral < 1.0 radian in the UV) without frequency modulation. The power spectrum is the azimuthal sum at each frequency of the square of the Fourier amplitudes, and the cutoff wave number corresponds to the *f*-number-limited spatial frequency. The power spectra are normalized to the dc component, and the $\sigma_{rms}$ is defined as the square root of the ratio of the power in the high frequencies (i.e., $k \geq 0.04\ \mu m^{-1}$ in the OMEGA target plane) to the power in the low frequencies (i.e., $k < 0.04\ \mu m^{-1}$). Solid/dashed lines represent measured/modeled power spectra. The predicted speckle structure shows excellent agreement with the measurement; hence, the zero accumulated *B*-integral shot serves as a calibration that demonstrates the capability of the UVETP diagnostic to fully resolve individual speckles.

image in Fig. 79.36(b)], while the pulses without frequency modulation have a highly modulated spatial intensity profile [see single pixel lineout overplotted on image in Fig. 79.36(a)]. The spatial resolution and overall detector size of the CCD restrict the UVETP measurement to slightly more than one-half of the laser-beam profile. As seen in Fig. 79.36, the laser beam is centered nominally on the photodetector, and 550 $\mu$m of the 950-$\mu$m (defined as the 95% enclosed energy contour) laser spot is sampled.

The temporal rate of 2-D SSD smoothing is deduced from the power spectra of the measured UVETP images of laser pulses having constant peak power and pulse lengths ranging from 100 ps to 3.5 ns. Power spectra calculated from measured UVETP images of (a) 100-ps and (b) 3-ns laser pulses smoothed with 2-D SSD are presented in Fig. 79.37. The time-dependent nature of 2-D SSD smoothing is evident in the measured results with lower measured values of $\sigma_{rms}$ for the longer pulse lengths. The low-wave-number power spectrum is determined by the spatial intensity envelope of the far field. The UVETP diagnostic was configured with a phase plate that produced a far-field spot with a super-Gaussian spatial intensity envelope $\left[I \sim \exp\left(r/r_0\right)^{2.5}\right]$ for these pulses.

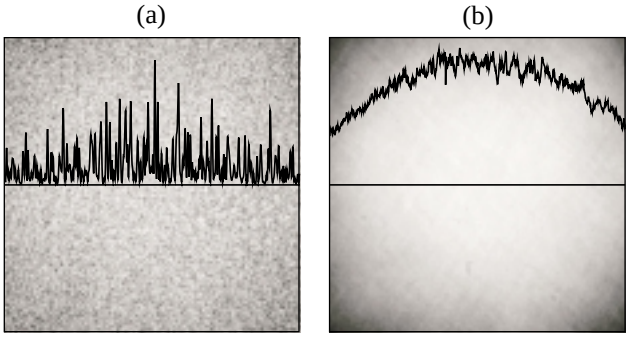


Figure 79.36
Measured UVETP images of 3.5-ns square laser pulses (a) without frequency modulation and (b) with 2-D SSD at $\Delta\nu_{UV} \approx 0.2$ THz. As demonstrated with the single pixel lineout through the center of the beam, the laser pulse with 2-D SSD has a smooth spatial intensity envelope, while the pulse without frequency modulation has a highly modulated spatial intensity profile. The spatial resolution and overall detector size of the CCD restrict the UVETP measurement to slightly more than one-half of the laser-beam profile. The laser beam is centered nominally on the photodetector, and 550 $\mu$m of the 950-$\mu$m laser spot (defined as the 95% enclosed energy contour) is sampled.

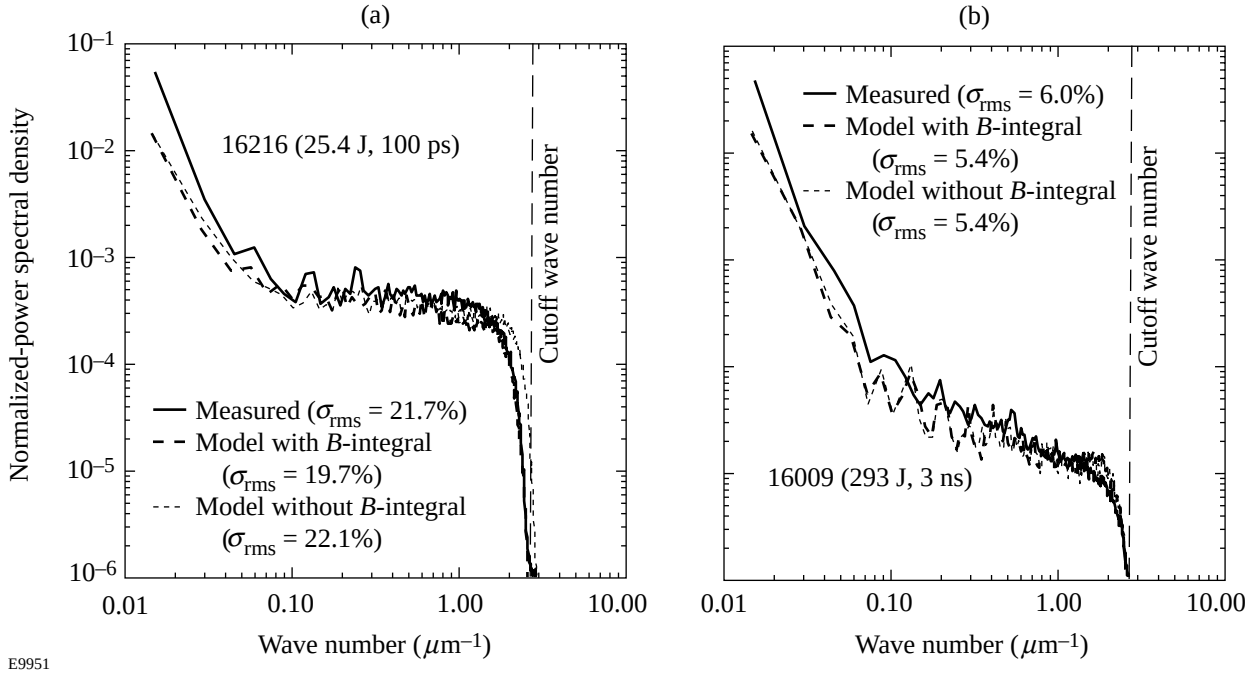


Figure 79.37
Power spectra calculated from UVETP images of (a) 100-ps and (b) 3-ns laser pulses with 2-D SSD. The thick, solid line represents the measured power spectrum. The thick, dashed line represents the time-dependent simulation that includes both the spatiotemporal behavior of the near-field irradiance and small-scale and whole-beam *B*-integral effects. The thin, dashed line represents a time-dependent model neglecting *B*-integral effects. Both models are in agreement with the measured results, and *B*-integral effects are negligible for all cases except for pulses without frequency modulation.

The 2-D SSD power spectra simulated with the time-dependent code (described in a previous section) with and without *B*-integral effects are plotted in Fig. 79.37. The *B*-integral effects are completely negligible as shown in this figure. The excellent agreement between the simulated power spectra and the measured spectra is clearly apparent in Fig. 79.37.

The measured temporal rate of 2-D SSD smoothing is shown in Fig. 79.38, which is a compilation of data from over 150 laser shots that clearly demonstrates the decrease in the measured $\sigma_{\text{rms}}$ with increasing pulse length. Statistical error bars are smaller than the symbols. The 3.5-ns pulse has the lowest measured $\sigma_{\text{rms}} = 6.0\%$. The measurement of the laser-irradiation nonuniformity for the 3.5-ns pulses without frequency modulation is also presented for comparison. The thin line is the time-integrated simulation of the single-beam irradiation nonuniformity $\sigma_{\text{rms}}$ that neglects the *B*-integral effects and assumes a static near field with a uniform irradiance. It is in agreement with the measured results (black circles), and it predicts that an asymptotic level of smoothing is reached just after 3 ns. The thick, solid line in Fig. 79.38 represents model predictions for the $\sigma_{\text{rms}}$:

$$\sigma_{\text{rms}} = \sqrt{\sigma_0^2\left(\frac{t_c}{t+t_c}\right)+\sigma_{\text{asymp}}^2}\,, \tag{3}$$

where $t_c = 1/\Delta\nu_{\text{UV}} = 5$ ps is the coherence time, $\Delta\nu_{\text{UV}}$ = 0.2 THz is the UV bandwidth, $t$ is the averaging time (i.e., pulse length), $\sigma_0$ is the initial laser nonuniformity, and $\sigma_{\text{asymp}}$ is the asymptotic level of 2-D SSD smoothing calculated from the time-integrated far-field simulation. This prediction adds the asymptotic levels of smoothing in quadrature to the model given in Ref. 14. The dashed line in Fig. 79.38 is a plot of Eq. (3) with the $\sigma_{\text{asymp}}$ set to zero. The deviation of the thick, solid line from the dashed line around 1 ns signifies that the beam smoothing is approaching its asymptotic limit. The asymptotic behavior can be observed in the measured values of $\sigma_{\text{rms}}$.

The dependence of the rate of smoothing on the wave number $k$ is examined in Fig. 79.39, where $\sigma_{\text{rms}}$ is plotted as a function of pulse length for the spectral wavelength ranges of $\lambda$ = 20-$\mu$m, $\lambda$ = 30-$\mu$m, $\lambda$ = 60-$\mu$m, and $\lambda$ = 150-$\mu$m wavelengths, corresponding to $k$ = 0.31 $\mu\text{m}^{-1}$, $k$ = 0.21 $\mu\text{m}^{-1}$, $k$ = 0.10 $\mu\text{m}^{-1}$, and $k$ = 0.04 $\mu\text{m}^{-1}$. Statistical error bars are again smaller than the symbols for the majority of the data. For OMEGA, this corresponds to spherical-harmonic modes of $\ell$ = 20 through 150, which are considered the most dangerous for ICF implosions.[5] Again the time-integrated 2-D SSD predictions are in good agreement with the experimental observations (*B*-integral effects are negligible here, too). The data have also been fitted using Eq. (3) with the approximation[5,21]

$$t_c = \left[\Delta\nu_{\text{UV}} \times \sin\left(k\delta/2\right)\right]^{-1}, \tag{4}$$

where $\delta$ is the separation between spectral modes. (For one color cycle $\delta$ corresponds to one-half of a speckle width,

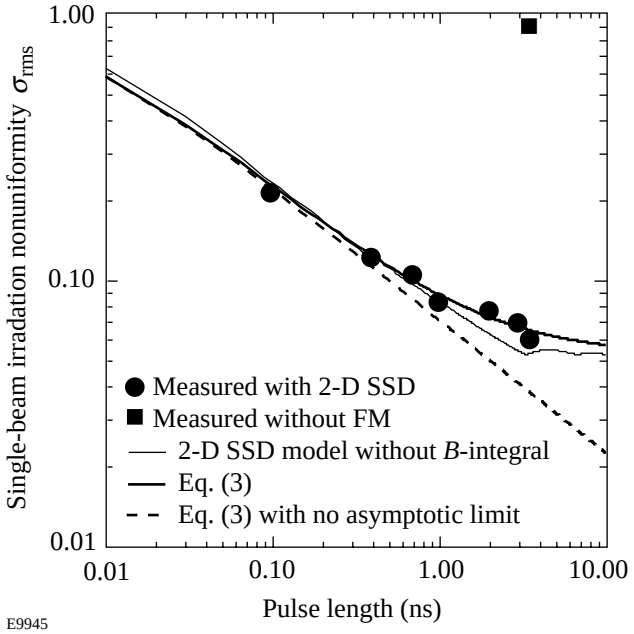


Figure 79.38
A compilation of data from over 150 laser shots demonstrates the temporal smoothing rates of 2-D SSD. Statistical error bars are smaller than the symbols. The 3.5-ns pulse has the lowest measured $\sigma_{\text{rms}}$ = 6.0%. The 3.5-ns pulse without frequency modulation is shown for comparison. The thin, solid line is the time-integrated simulation of the single-beam irradiation nonuniformity $\sigma_{\text{rms}}$ that neglects the *B*-integral effects and assumes a static near field with a uniform irradiance. The thick, solid line represents the model predictions for $\sigma_{\text{rms}}$ using Eq. (3). The dashed line is the model prediction for $\sigma_{\text{rms}}$ with $\sigma_{\text{asymp}} = 0$.

i.e., $\delta = F\lambda/D = 2.35\ \mu$m.) In a manner similar to Fig. 79.38, the case neglecting the asymptotic behavior of Eq. (3) is also plotted in Fig. 79.39. The initial value of the laser nonuniformity $\sigma_0$ for each spectral range was determined by taking the average value of the measured $\sigma_{rms}$ for shots without frequency modulation. The data in Fig. 79.39 demonstrate that the shorter wavelengths ($\lambda = 20\ \mu$m) are smoothed more effectively than the longer wavelengths. It can also be observed that the longer-wavelength modes approach their asymptotic limits sooner than the shorter ones. Only a small amount of smoothing is observed for $\lambda = 150$-$\mu$m wavelength (corresponding to $l \approx 20$), which is in agreement with the prediction.

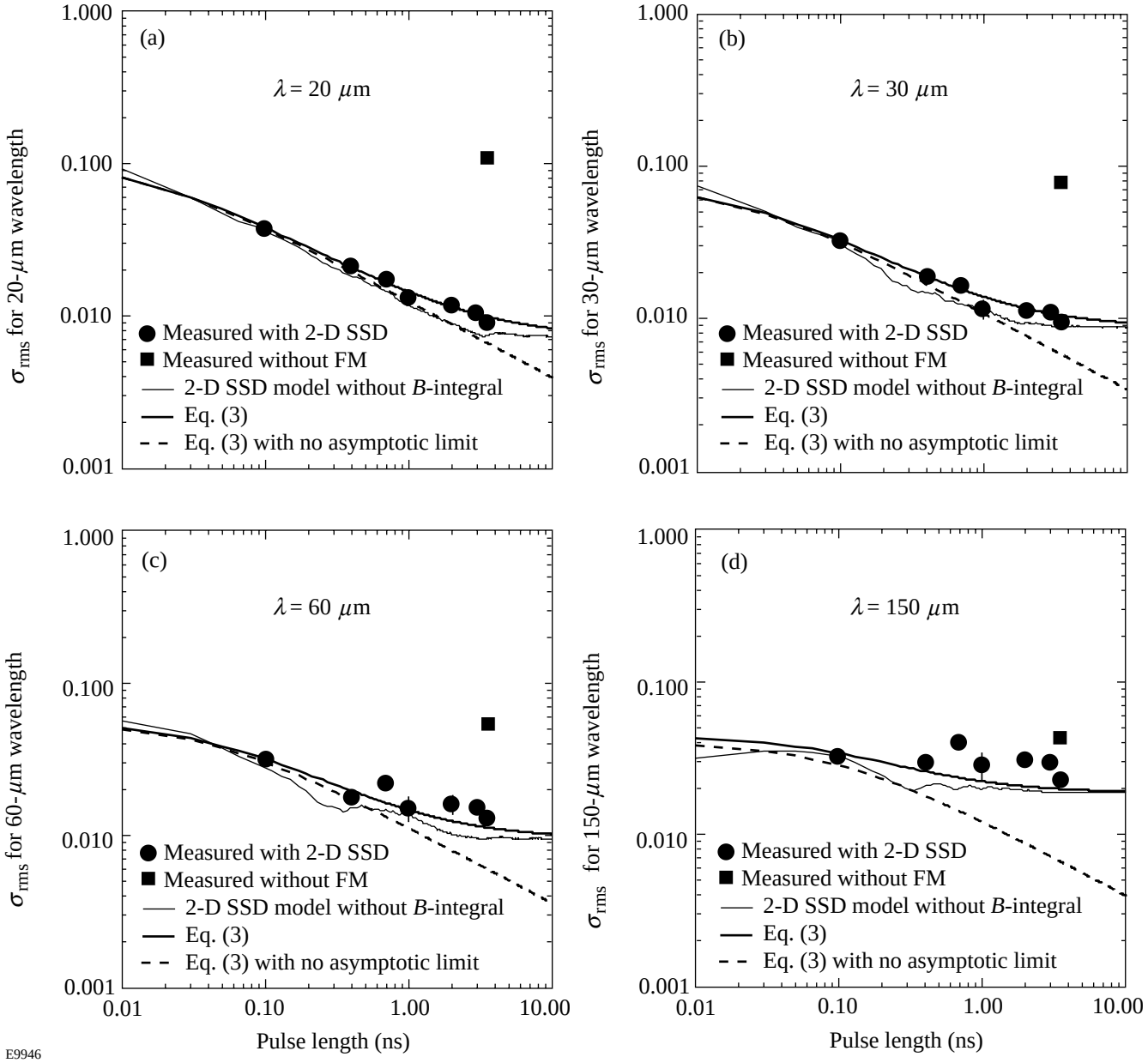


Figure 79.39
Temporal smoothing rates for specific spatial wavelengths (a) $\lambda = 20\ \mu$m ($k = 0.31\ \mu$m$^{-1}$), (b) $\lambda = 30\ \mu$m ($k = 0.21\ \mu$m$^{-1}$), (c) $\lambda = 60\ \mu$m ($k = 0.10\ \mu$m$^{-1}$), and (d) $\lambda = 150\ \mu$m ($k = 0.04\ \mu$m$^{-1}$). Statistical error bars are smaller than the symbols for the majority of the data. The 2-D SSD predictions are in good agreement with the experimental observations. The thick, solid line represents the model predictions for $\sigma_{rms}$ using Eqs. (3) and (4). The dashed line is a model prediction for $\sigma_{asymp} = 0$. The thin, solid line is the predicted $\sigma_{rms}$ from a 2-D SSD simulation using a static near field with a uniform irradiance and neglecting *B*-integral effects.

## Conclusion

Direct-drive ICF experiments require a laser system with excellent irradiation uniformity. Two-dimensional smoothing by spectral dispersion is currently the best mechanism for reducing laser-beam nonuniformities for high-power/energy glass lasers. UVETP images of a single OMEGA laser beam were recorded to quantify the single-beam irradiation nonuniformity. The smoothing rate of 2-D SSD (with the current UV bandwidth of $\Delta\nu_{UV} \approx 0.2$ THz) was determined by analyzing the power spectra of measured UVETP images of laser pulses having constant peak power and pulse lengths ranging from 100 ps to 3.5 ns. Simulated 2-D SSD power spectra and temporal smoothing rates are in excellent agreement with the experimental data and permit confident extrapolation to larger laser systems and higher UV bandwidths.

## ACKNOWLEDGMENT

The authors appreciate the support of Sam Morse and the entire OMEGA engineering staff, especially Chris Cotton for the design of the CCD optics, Charles Kellogg for the installation of the diagnostic, and Keith Thorp, Per Adamson, Ray Huff, Matt Kamm, Dave Kuhn, and Howard Ammenheuser for the operation and alignment of the diagnostic. This work was supported by the U.S. Department of Energy Office of Inertial Confinement Fusion under Cooperative Agreement No. DE-FC03-92SF19460, the University of Rochester, and the New York State Energy Research and Development Authority. The support of DOE does not constitute an endorsement by DOE of the views expressed in this article.

## REFERENCES

1. C. P. Verdon, Bull. Am. Phys. Soc. **38**, 2010 (1993).

2. S. E. Bodner, D. G. Colombant, J. H. Gardner, R. H. Lehmberg, S. P. Obenschain, L. Phillips, A. J. Schmitt, J. D. Sethian, R. L. McCrory, W. Seka, C. P. Verdon, J. P. Knauer, B. B. Afeyan, and H. T. Powell, Phys. Plasmas **5**, 1901 (1998).

3. D. K. Bradley, J. A. Delettrez, and C. P. Verdon, Phys. Rev. Lett. **68**, 2774 (1992); J. Delettrez, D. K. Bradley, and C. P. Verdon, Phys. Plasmas **1**, 2342 (1994); J. D. Kilkenny, S. G. Glendinning, S. W. Haan, B. A. Hammel, J. D. Lindl, D. Munro, B. A. Remington, S. V. Weber, J. P. Knauer, and C. P. Verdon, Phys. Plasmas **1**, 1379 (1994); R. Epstein, J. Appl. Phys. **82**, 2123 (1997); V. A. Smalyuk, T. R. Boehly, D. K. Bradley, V. N. Goncharov, J. A. Delettrez, J. P. Knauer, D. D. Meyerhofer, D. Oron, and D. Shvarts, Phys. Rev. Lett. **81**, 5342 (1998).

4. S. Skupsky, R. W. Short, T. Kessler, R. S. Craxton, S. Letzring, and J. M. Soures, J. Appl. Phys. **66**, 3456 (1989).

5. Laboratory for Laser Energetics LLE Review **69**, 1, NTIS document No. DOE/SF/19460-152 (1996); S. Skupsky and R. S. Craxton, Phys. Plasmas **6**, 2157 (1999).

6. J. E. Rothenberg, J. Opt. Soc. Am. B **14**, 1664 (1997).

7. T. J. Kessler, Y. Lin, J. J. Armstrong, and B. Velazquez, in *Laser Coherence Control: Technology and Applications*, edited by H. T. Powell and T. J. Kessler (SPIE, Bellingham, WA, 1993), Vol. 1870, pp. 95–104.

8. Y. Lin, T. J. Kessler, and G. N. Lawrence, Opt. Lett. **21**, 1703 (1996).

9. Y. Kato, unpublished notes (1984); K. Tsubakimoto *et al.*, Opt. Commun. **91**, 9 (1992); K. Tsubakimoto *et al.*, Opt. Commun. **103**, 185 (1993).

10. Laboratory for Laser Energetics LLE Review **45**, 1, NTIS document No. DOE/DP40200-149 (1990); T. E. Gunderman, J.-C. Lee, T. J. Kessler, S. D. Jacobs, D. J. Smith, and S. Skupsky, in *Conference on Lasers and Electro-Optics*, Vol. 7, 1990 OSA Technical Digest Series (Optical Society of America, Washington, DC, 1990), p. 354.

11. T. R. Boehly, V. A. Smalyuk, D. D. Meyerhofer, J. P. Knauer, D. K. Bradley, R. S. Craxton, M. J. Guardalben, S. Skupsky, and T. J. Kessler, J. Appl. Phys. **85**, 3444 (1999).

12. J. Paisner *et al.*, Laser Focus World **30**, 75 (1994).

13. M. Desselberger *et al.*, Phys. Rev. Lett. **68**, 1539 (1992); S. G. Glendinning, S. V. Weber, P. Bell, L. B. DaSilva, S. N. Dixit, M. A. Henesian, D. R. Kania, J. D. Kilkenny, H. T. Powell, R. J. Wallace, P. J. Wegner, J. P. Knauer, and C. P. Verdon, *ibid*. **69**, 1201 (1992); D. H. Kalantar, M. H. Key, L. B. DaSilva, S. G. Glendinning, J. P. Knauer, B. A. Remington, F. Weber, and S. V. Weber, *ibid*. **76**, 3574 (1996); S. G. Glendinning, S. N. Dixit, B. A. Hammel, D. H. Kalantar, M. H. Key, J. D. Kilkenny, J. P. Knauer, D. M. Pennington, B. A. Remington, R. J. Wallace, and S. V. Weber, Phys. Rev. E **54**, 4473 (1996); R. J. Taylor *et al.*, Phys. Rev. Lett. **79**, 1861 (1997); D. H. Kalantar, M. H. Key, L. B. Da Silva, S. G. Glendinning, B. A. Remington, J. E. Rothenberg, F. Weber, S. V. Weber, E. Wolfrum, N. S. Kim, D. Neely, J. Zhang, J. S. Wark, A. Demir, J. Lin, R. Smith, G. J. Tallents, C. L. S. Lewis, A. MacPhee, J. Warwick, and J. P. Knauer, Phys. Plasmas **4**, 1985 (1997); S. G. Glendinning, S. N. Dixit, B. A. Hammel, D. H. Kalantar, M. H. Key, J. D. Kilkenny, J. P. Knauer, D. M. Pennington, B. A. Remington, J. Rothenberg, R. J. Wallace, and S. V. Weber, Phys. Rev. Lett. **80**, 1904 (1998); T. R. Boehly, V. A. Smalyuk, O. Gotchev, J. P. Knauer, D. D. Meyerhofer, D. K. Bradley, J. A. Delettrez, S. Skupsky, and R. P. J. Town, Bull. Am. Phys. Soc. **43**, 1664 (1998).

14. R. H. Lehmberg and S. P. Obenschain, Opt. Commun. **46**, 27 (1983); R. H. Lehmberg, A. J. Schmitt, and S. E. Bodner, J. Appl. Phys. **62**, 2680 (1987).

15. T. R. Boehly, D. L. Brown, R. S. Craxton, R. L. Keck, J. P. Knauer, J. H. Kelly, T. J. Kessler, S. A. Kumpan, S. J. Loucks, S. A. Letzring, F. J. Marshall, R. L. McCrory, S. F. B. Morse, W. Seka, J. M. Soures, and C. P. Verdon, Opt. Commun. **133**, 495 (1997).

16. D. C. Brown, in *High-Peak-Power Nd:Glass Laser Systems*, edited by D. L. MacAdam, Springer Series in Optical Sciences (Springer-Verlag, Berlin, 1981), Vol. 25, p. 45.

17. Laboratory for Laser Energetics LLE Review **78**, 62, NTIS document No. DOE/SF/19460-295 (1999). Copies may be obtained from the National Technical Information Service, Springfield, VA 22161.

18. Photometrics Ltd., Tucson, AZ 85706.

19. Color filter glass, Schott Glass Technologies, Inc., Duryea, PA 18642.

20. Color filter glass, Hoya Corporation, Tokyo 161-8525, Japan.

21. S. Skupsky, LLE, private communication (1999).